Electrochimica Acta 360 (2020) 136990

Contents lists available at ScienceDirect

Electrochimica Acta

journal homepage: www.elsevier.com/locate/electacta

Electrolytic characteristics of ammonia oxidation in real aquaculture water using nano-textured mono-and bimetal oxide catalysts supported on graphite electrodes

Yu-Jen Shih[a,*], Shih-Hsuan Huang[a], Ching-Lung Chen[b,c], Cheng-Di Dong[d], Chin-Pao Huang[e,*]

[a] Institute of Environmental Engineering, National Sun Yat-sen University, Kaohsiung, Taiwan
[b] Department of Safety, Health and Environmental Engineering, Ming Chi University of Technology, New Taipei City, Taiwan
[c] Center for Environmental Sustainability and Human Health, Ming Chi University of Technology, New Taipei City, 24301, Taiwan
[d] Department of Marine Environmental Engineering, National Kaohsiung University of Science and Technology, Kaohsiung, Taiwan
[e] Department of Civil and Environmental Engineering, University of Delaware, Newark DE 19716, United States

ARTICLE INFO

Article history:
Received 18 July 2020
Revised 17 August 2020
Accepted 20 August 2020
Available online 2 September 2020

Keywords:
Ammonia nitrogen
Aquaculture water
Breakpoint chlorination
Electrochemical oxidation
Spinel oxides

ABSTRACT

Electrodes were made by electrochemically deposition of mono-metal (Sn, Mn, Pb, and Co) and bimetal (Co-Zn and Co-Ni) oxides on graphite support using metal tartrate precursor in alkaline solution (pH 12). Results of XRD, XPS, and SEM analyses indicated that the nano-textured oxides were consisted of mineral phases, namely, cassiterite (SnO_2), birnessite (δ-MnO_2), and plattnerite (β-PbO_2), and spinel-type cobalt oxides (Co_3O_4, $ZnCo_2O_4$, and $NiCo_2O_4$). Cobalt oxide electrode exhibited high chlorine yield because of improved electrical capacitance and transfer coefficient. The rate of chlorine evolution on CoO/G, CoZnO/G, and CoNiO/G electrodes was $>2 \times 10^{-4}$ min^{-1}, which was almost one order magnitude greater than that of other mono-metal oxides ($3–8 \times 10^{-5}$ min^{-1}). The removal of ammonia nitrogen was > 90% under breakpoint chlorination for the treatment of real aquaculture wastewater ($[NH_4^+] \approx 3$ mg-N/L or 2.1×10^{-4} M, $[Cl^-] = 0.37$ M, current density = 3.5 mA/cm^2).

1. Introduction

Aquaculture fishery is an important economic activity in southwestern Taiwan. The excreta of aquatic organisms and the microbial decomposition of unconsumed feed and feces, rapidly accumulate ammonia nitrogen (NH_4^+-N) in the fish ponds [1,2]. The toxicity of ammonia increases with increasing pH because ammonia is the major species, which implies that temperature and salinity of source water are factors controlling ammonia toxicity to fish [3]. Ammonia can damage gill, reduce oxygen-carrying capacity of blood, and affect osmoregulation at very low level [4]. At concentrations higher than 0.05 mg-N/L, ammonia species, i.e., NH_3, can cause respiratory stress to fish, which renders fish more vulnerable to parasitic and infectious agents. Besides, intensive ammonia development in the aquaculture also impacts the eco-environmental system, e.g., chemoautotrophic bacteria (*Nitrosomonas* and *Nitrobacter*) tend to oxidize ammonium (NH_4^+-N) to nitrite (NO_2^--N) and nitrate (NO_3^--N). The assimilation of the nitrogen oxyanions as nutrients by aquatic plants, i.e., algae and phytoplankton, leads to eutrophication which perturbs the ecostability [5]. Currently, Taiwan Environmental Protection Agency (EPA) has established ammonia-nitrogen concentration of 0.3 mg-N/L for class 2 aquaculture water quality. The European Union has set a total ammonia nitrogen limit of 1 mg-N/L for fish culturing, specifically salmonid and cyprinid (78/659/EEC). According to US EPA, the acute level of ammonia nitrogen is 17 mg-N/L. Molecular ammonia less than 0.020 mg-N/L is considered safe for fish reproduction. Canada has recommended a water quality of 0.019 mg-N/L as chronic toxic level [6]. Moreover, NH_4^+ concentration as low as 1–2 mg-N/L triggers eutrophication in oligotrophic waters [7].

Recirculating Aquaculture System (RAS), consisting of several aerated fish tanks in-series, is typically used in the closed culture of fishery, where a number of biofilters are used to maintain the quality of the circulating water. However, the biological method may be ineffective in treating saline water [8,9]. Control of ammonia in fish culture water has been widely investigated using selective ion exchange [10], flocculation [11], chemical oxidation [12], and membrane bioreactors [13]. The addition of chemical additives,

* Corresponding authors.
E-mail addresses: mcdyessjin@gmail.com (Y.-J. Shih), huang@udel.edu (C.-P. Huang).

https://doi.org/10.1016/j.electacta.2020.136990
0013-4686/

sludge production, high energy demand contributed to high operation cost and secondary pollution that required intensive post-treatment. There are current interests on new methods for ammonium removal in aquaculture wastewater. Direct oxidation using single-crystal Pt or Pt-based alloys has been studied in the field of ammonia-fed fuel cell [14-16]; however, Shih et al. demonstrated that the selectivity of N_2 formation from dilute ammonia solution by electrochemical oxidation on non-noble metallic electrodes was low [17,18].

Indirect oxidation converted ammonia to chloramines at specific chlorine to ammonia mole ratio [19]. Breakpoint chlorination was necessary to obtain free chlorine residual for better disinfection operation in which all the ammonia was completely oxidized to N_2 [20]. The average level of NH_4^+-N was around 3–10 mg/L in untreated aquaculture wastewater collected from southern Taiwan. Since the seawater used in fishery farms has high Cl^-concentration (~1000 mg/L), electrochemical chlorination will be an ideal approach for *in-situ* de-ammonification. Noble metals/metal oxides (Pt, Pd, Ru, Rh, Au) have high chloride adsorption specificity and wide application in the chlor-alkali industry because of low chlorine evolution potential (CEP) and long service life [21-24]. IrO_2/Ti and boron-doped diamond are known commercial electrodes that have been used to generate reactive chlorine for electrochemical water treatment and disinfection [25, 26]. Replacement of costly noble metals such as graphite and PbO_2 by cost anodes of comparable catalytic efficiency has also gained substantial interest in the field [27, 28]. High activity in chlorine generation in a short hydraulic retention time without producing excessive chlorine (which will cause the formation of chlorinated species, i.e., DBPs) [29] is important attribute for the design of effective ammonia treatment systems. In this work, graphite-supported metal oxides were fabricated for the removal of ammonia from synthetic brine and real aquaculture waters at dilute ammonia concentration. Non-noble metals, specifically, Sn, Mn, Pb, and Co, and bimetal, namely, Co-Zn and Co-Ni, oxides, were synthesized by electrodeposition. It was hypothesized that the type of metal would affect the physicochemical properties, such as morphology and electro-catalytic activity of the metallic oxides, which in turn would control breakpoint chlorination kinetics. The goal was to study *in-situ* chlorine generation for ammonia (exactly ammonium ion) removal from saline water used in fish farming operations.

2. Materials and methods

2.1. Graphite-based electrodeposition of metal oxide electrodes

The substrate for metal oxide deposition was graphite plate (thickness = 5 mm) purchased from Great Carbon Co., Ltd., Taiwan. The raw graphite was polished with an ultrafine sandpaper (P400, 3 M), followed by rinsing with acetone, and then acid etching in 1 M H_2SO_4 solution in a ultrasonic bath to remove adhesive and grease. Fig. S1 shows the preparation procedure for metal oxide supported on graphite electrodes. To achieve better conductivity and stability of the electrode, a thin interconnection layer of tin oxide was added to the graphite surface first by dipping the graphite plate in a mixture solution of 0.05 M $SnCl_4$ and 2 M HCl for 5 times, drying at 105 °C, and then calcining at 500 °C in atmospheric air for 1 h [30]. The electrolytic bath was prepared by dissolving a given amount of metal salt, including $CoCl_2{\cdot}6H_2O$, $MnSO_4{\cdot}H_2O$ (Sigma-Aldrich, USA), $Pb(NO_3)_2$ (SHOWA, Japan), $SnCl_2{\cdot}H_2O$, $Ni(NO_3)_2$ (Alfa Aesar, USA), and $ZnSO_4{\cdot}7H_2O$ (PANREAC) to give a final concentration of 10^{-2} M in alkaline solution (pH 12) in the presence of 0.15 M L(+)-Tartaric acid ($C_4H_6O_6$, Alfa Aesar, USA) as chelating agent. The metal oxide was deposited on the graphite electrode that was previously coated a thin layer of tin oxide (with another plain graphite plate as cathode) under constant current density of 30 mA/cm^2 for 2 h. After deposition, the metal oxide-coated graphite electrodes (MO/G, M denoted metal including Co, Mn, Sn, Pb, Co-Zn, and Co-Ni) was rinsed with deionized water to remove residual salt before use.

Table 1
Composition of synthetic sea salt.

Major cations	mg L^{-1}	Major anions	mg L^{-1}
Na^+	9200 – 9700	Cl^-	17,000 – 18,000
Mg^{2+}	1300 – 1400	SO_4^{2-}	2250 – 2500
K^+	350 – 400	Br^-	20 – 40
Ca^{2+}	380 – 430		

Stock solution was prepared by dissolving 35 g salt sample in 1 liter of deionized water; pH 8.5, [Cl^-] ~ 0.5 M).

2.2. Electrochemical chlorine yield and ammonia oxidation

Cyclic voltammetry (CV) was used to study the chloride redox characteristics on MO/G as the working electrode (effective area = 3 cm^2), using potentostat (CHI611C, CH Instruments, Inc., Austin, TX, USA) in 0.1 M of Na_2SO_4 as supporting electrolyte. A graphite plate with the same dimension as the working electrode was the counter electrode. The reference electrode was Ag/AgCl. The *i-E* response of voltammetry in the presence of NaCl was recorded by scanning potential at specific rates (ω, V/s).

Batch constant current experiments were performed under different current density and initial chloride concentration. To assess the ability of MO/G electrodes, ISTA Coral Sea Salt was diluted to prepare the chloride electrolyte. The composition of synthetic seawater was listed in Table 1. The electrochemical reactor was constructed with two polymethyl methacrylate (PMMA) plates, intercalated between electrodes and a spacer at a distance of 0.5 cm to separate the two electrodes. The MO/G anode was cut into a dimension of 5 × 5 cm^2 (total effective area ~25 cm^2). A graphite plate of the same dimension as the MO/G was used as the cathode. The simulated water using $(NH_4)_2SO_4$ and real aquaculture wastewater were prepared as ammonium containing solutions. The real wastewater sample was collected from fishery ponds located in Mido District, Kaohsiung, Taiwan, where brackish water was fed to farm fish. Table 2 gives the chemical composition of real fish farm water. Water samples were taken at specific time intervals to analyze the concentration of chlorine and ammonia. The current efficiency (η,%) in terms of chlorine yield, and the percentage of ammonium removal (C/C_0,%), were calculated according to the following equations [31, 32]:

$$\eta(\%) = \frac{nF \times [Cl_2] \times V}{I \times t \times Mw} \times 100 \quad (1)$$

$$\frac{C}{C_o}(\%) = \frac{\left[NH_4^+\right]_t}{\left[NH_4^+\right]_o} \quad (2)$$

where [Cl_2] stands for the chlorine yield in mg-Cl_2/L at time t. n represents the number of electron transfer for converting Cl^- to Cl_2, i.e., 2; F is the Faraday constant (96,485 C/mol); V is reaction volume (0.8 L); I is the applied current; and Mw is the molecular weight of chlorine (71 g/mol).

2.3. Chemical analysis of chlorine and nitrogen

The concentration of free chlorine was analyzed by the N, N–diethyl-p-phenylenediamine (DPD) colorimetric method (Hach Method 8021, USEPA) [33]. The residual chlorine reacts with specific amount of $KMnO_4$ which was calibrated using DPD regent; the produced red color was measured by colorimetry at 520 nm using a spectrophotometer. Ammonium ion was analyzed via the

Table 2
Quality of real aquaculture water sampled from Mituo District, Kaohsiung, Taiwan.

Major cations	mg L^{-1}	meq L^{-1}	Major anions	mg L^{-1}	meq L^{-1}
Na^+	9335±1089	405.8 ± 47.4	Cl^-	11,551±2198	326.3 ± 62.1
K^+	403.5 ± 75.7	10.3 ± 1.94	NO_3^-	1.53±0.65	0.109±0.05
Ca^{2+}	323.5 ± 81.3	16.2 ± 4.1	NO_2^-	0.17±0.04	0.012±0.003
Mg^{2+}	1044±143	85.9 ± 11.6	SO_4^{2-}	2953±261	184.6 ± 13.5
NH_4^+	3.69±0.72	0.26±0.05	Alkalinity	108.6 ± 16.2	1.78±0.26
		518.6 ± 65.1			512.8 ± 48.8
			TOC	97.6	

indophenol method at 630 nm according to the Berthelot reaction (Method 350.1, USEPA) [34], in which the NH_4^+-N reacted with phenoxide ($NaOC_6H_5 \bullet 3H_2O$) and hypochlorite (NaClO) using nitroprusside ($Na_2[Fe(CN)_5NO]$) (Riedel-deHaën AG, Germany) catalyst. A flow injection analyzer (FIA, Lachat's Quik Chem 8500 Series 2, Love land, Colorado, USA) was used to automatically measure the concentration of aqueous nitrogen species (NO_3^--N, NH_4^+-N, NO_2^--N). Deionized water, which has been purified with a laboratory-grade RO-ultrapure water system (resistivity >18.18 MΩ-cm), was used for the preparation of all solutions.

2.4. Surface characterization of metal oxide/graphite electrodes

The morphology and the elemental components of MO/G electrodes were analyzed using scanning electron microscope (SEM, JSM-6700F, JEOL) integrated with an energy dispersive spectroscopy (EDS, INCA400, OXFORD).The crystallographic structure was characterized by X-ray diffraction (XRD, DX III, Rigaku Co., Tokyo, Japan) under conditions: Cu Kα source (λ = 1.5406 Å), scan rate = 0.06° s, incidence angle = 20–85° (2θ). X-ray photoelectron spectroscopy (XPS, PHI 5000 VersaProbe Physical Electronics, Inc., USA) was used to determine the chemical state with a monochromatic Al Kα X-ray source (1487 eV).

3. Results and discussion

3.1. Surface characteristics of MO-G electrodes

Results of XRD patterns in Fig. 1 show the crystal structure of MO/G electrodes. The metal oxides deposited on graphite (G), namely, SnO/G, MnO/G, and PbO/G, mainly were mineral crystallinities, cassiterite (SnO_2), birnessite (δ-MnO_2), and plattnerite (β-PbO_2), respectively. Electrodeposition has been reported to produce amorphous SnO_2, with a broad signal of (110) diffraction at 2θ = 26° on the noisy background [35]. The mixing of manganite, MnOOH (111) at 2θ = 26°, and birnessite diffractions proved the Mn(III)/Mn(IV) transition during electrochemical redox reaction [36]. The undefined peaks in PbO/G sample (Fig. 1) could be attributed to α-PbO_2, which has been previously reported to be co-existing with β-PbO_2 when deposition was performed in alkaline solution [17]. By contrast, CoO/G electrode was constituted of Co_3O_4, suggesting that co-precipitation of Co(II) and Co(III) occurred on the G surface [37]. Various spinel-type binary metal oxides, $A^{(2+)}B_2^{(3+)}O_4$, A being divalent metal ion (Zn^{2+}, Ni^{2+}, Mn^{2+}, and Cu^{2+}) and B being trivalent metal ions (Co^{3+}, Fe^{3+}, and Mn^{3+}) have been investigated as pseudocapacitors [38]. In this work, the crystal structure of CoZnO/G, CoNiO/G, and CoO/G, identified as $ZnCo_2O_4$, $NiCo_2O_4$, and Co_3O_4, respectively, were used to study the electrochemical property of spinel oxide. Fig. 2 shows the SEM image of metal oxide electrodes. The raw graphite electrode was normally fabricated with carbon flakes (Fig. 2a), which exhibited a rougher surface after coated with middle layer of tin oxide (Fig. 2b). After electrodeposition, the size of SnO_2, in a form of crystal cluster on SnO/G, increased (Fig. 2c). The particles in pyramidal shape on PbO/G (Fig. 2d) indicated the presence of

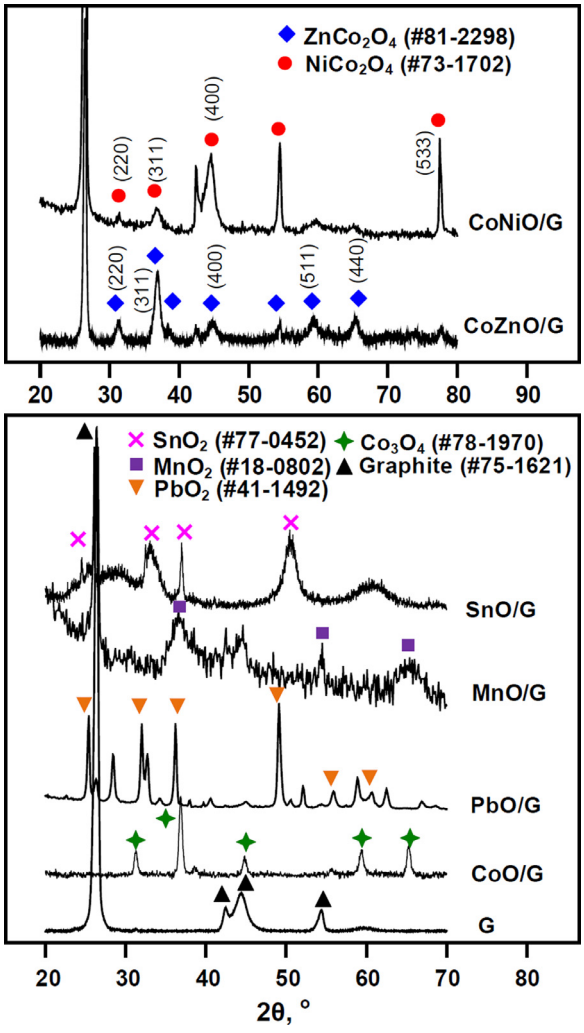

Fig. 1. XRD patterns of graphite-supported metal oxide electrodes.

good crystallinity of β-PbO_2 which was the same as lead dioxide previously synthesized for direct ammonium ion oxidation [17]. The MnO_2 layer on MnO/G comprised of nano-whisker crystallites (Fig. 2e), which had similar shape as tiny platelets of birnessite prepared by cycling voltammetric method [36]. Fig. 2f-2h shows the nano-particulate morphology of spinel oxides which did not differ significantly from each other except with particle size following the order: CoNiO > CoZnO > CoO.

Fig. 3 presents XPS spectra of Sn 3d, Pb 4f, Mn 2p, and Co 2p orbitals on MO/G electrodes. Results clearly showed the oxidation state of metals in the oxide electrodes. Anodic electrodeposition altered the oxidation state of metals to some extent. A significant portion of 93% tin in SnO/G was in the Sn(IV) state at 495.6 eV of Sn $3d_{3/2}$ orbital [39]. Nevertheless, in PbO/G, the mole fraction of

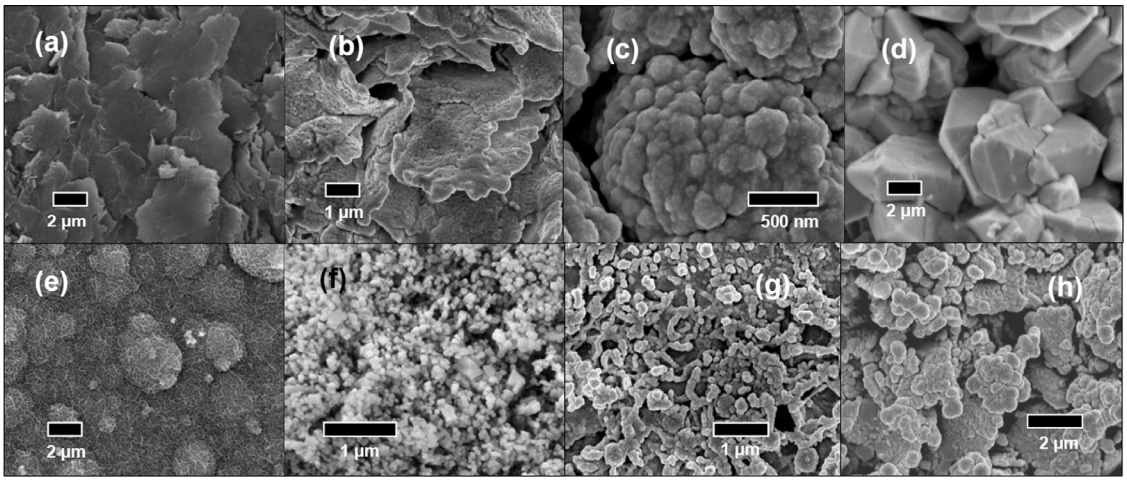

Fig. 2. SEM micromorphology of metal oxide electrodes (a) G, (b) Sn middle layer, (c) SnO/G, (d) PbO/G, (e) MnO/G, (f) CoO/G, (g) CoNiO/G, and (h) CoZnO/G.

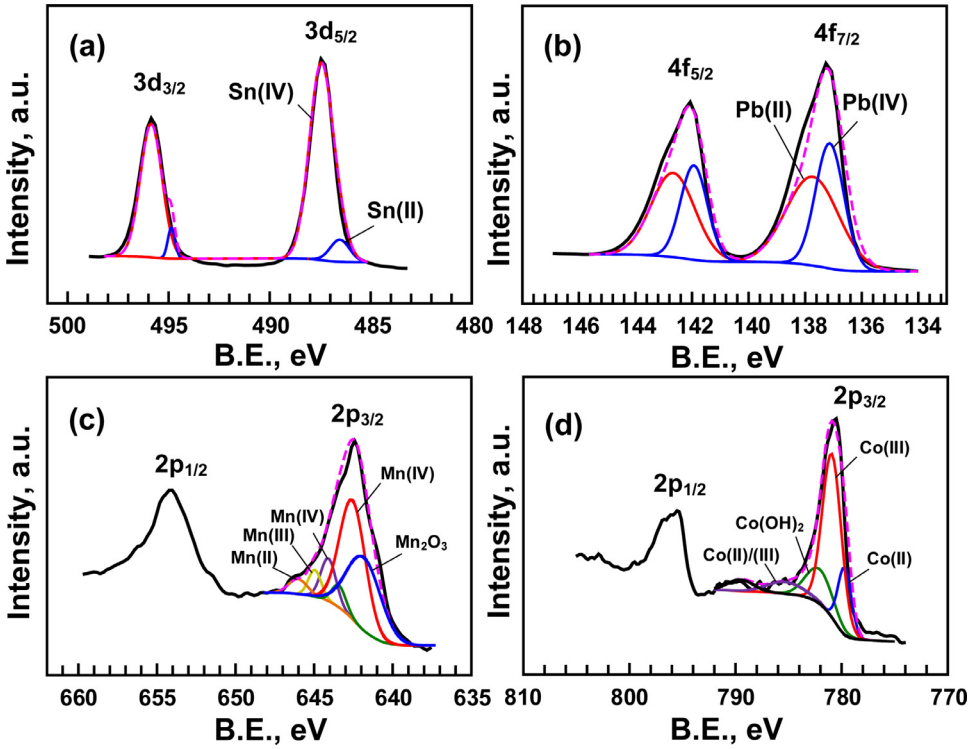

Fig. 3. Binding energies of XPS spectrum in regions of (a) Sn 3d, (b) Pb 4f, (c) Mn 2p, and (d) Co 2p orbitals for SnO/G, PbO/G, MnO/G, and CoO/G electrodes, respectively.

Pb(II) and Pb(IV) $4f_{5/2}$ at 142.7 and 141.9 eV were comparable, at 59% and 41%, respectively [16]. Several oxidation states of Mn and Co existed in the oxide electrodes; in MnO/G, the band at 645.9, 644.9, and 642.7 eV were $2p_{3/2}$ orbitals of Mn(II), Mn(III) and Mn(IV), respectively [40]. Mn(IV) as birnessite phase and Mn(III) (at 641.9 eV) in the form of Mn_2O_3 accounted for 43.2% and 34.6%, respectively. Co $2p_{3/2}$ in Co(II) and Co(III) states were at the band energy of 780 eV and 782.2 eV for CoO and $Co(OH)_2$, and 781.4 eV and 785.2 eV for CoOOH and Co_3O_4, respectively [40]. The fraction of 32.4% for Co(II) and 55% for Co(III) suggested the co-existence of $Co(OH)_2$ and Co_3O_4/CoOOH in CoO/G.

3.2. Electrochemical properties of MO-G electrodes

The behavior of electrochemical charging and chloride redox reaction over MO/G electrodes was assessed using cyclic voltammetry (CV). Fig. S2 gives CV curves of inert electrolyte (Na_2SO_4) that described the redox reactions of metal oxides. For an ideal polarizable electrode, the symmetrical *E-i* response by sweeping voltage in the anodic and cathodic directions should be attributed to the non-faradaic charging of SO_4^{2-} and Na^+, respectively, as electric double-layer (EDL) capacitance. For PbO/G, MnO/G, and CoO/G electrodes, an obvious couple of faradaic redox current was brought by reversible transition of metal oxidation state as pseudocapacitance [41]. Based on the current (I, A) evolved by scanning potential at a specific rate (v, V/s), i.e., voltammetry measurement, the differential capacitance of the electrode (C, F) was calculated by the following equation:

$$C \equiv \frac{\partial \sigma}{\partial E} = \frac{I \times dt}{dE} = \frac{I}{v} \quad (3)$$

where σ is the charge density (C), E is the working potential (V vs. Ag/AgCl) and v is the scan rate (V/s). The capacitive charging in

Table 3
Electrochemical parameters.

Samples	E_{pzc}, V	C_{pzc}, mF/cm^2	D_{Cl}, cm^2/s	*b*, V/dec	α
G	0.735	11.4	3.65×10^{-8}	0.123	0.48
SnO/G	0.675	22.4	1.00×10^{-6}	0.193	0.31
MnO/G	0.875	52.9	1.45×10^{-7}	0.273	0.22
PbO/G	1.095	52.6	7.45×10^{-7}	0.209	0.28
CoO/G	0.885	122	2.85×10^{-7}	0.074	0.80
IrO_2/Ti	0.645	25.6	1.34×10^{-7}	0.222	0.27
CoZnO/G	0.665	112	1.49×10^{-7}	0.085	0.69
CoNiO/G	0.725	119	8.67×10^{-7}	0.088	0.67

$E_{pzc:}$ electrode potential at point of zero charge; C_{pzc}: electric capacitance at p.z.c; D_{Cl}: diffusion coefficient of chloride ion; *b*: Tafel slope; α: transfer coefficient estimated over metal oxides.

anodic and cathodic direction were ascribed to anodic C_a and cathodic C_c, respectively [42]; that is, C_c is equal but opposite in sign to C_a at the point of zero charge, E_{pzc}, that is, the eletrocapilary maximum [43]:

$$C_a = -C_c = C_{pzc} \ @ \ E = E_{pzc} \tag{4a}$$

$$C_a = \frac{\partial \sigma_+}{\partial E} = \frac{I_a}{\nu} \tag{4b}$$

$$C_c = \frac{\partial \sigma_-}{\partial E} = -\frac{I_c}{\nu} \tag{4c}$$

Fig. S3 gives the differential capacitance as a function of E-E_{pzc} of various MO/G electrodes. Table 3 presents the minimum C_{pzc} of various MO/G electrodes in the presence of 0.1 M Na_2SO_4. The minimum C_{pzc} followed the order: CoO/*G* ≈ CoZnO/*G* ≈ CoNiO/G (~110 mF/cm^2) > MnO/*G* ≈ PbO/G (~50 mF/cm^2) > IrO_2 ≈ SnO/G (~25 mF/cm^2) > *G* (~10 mF/cm^2). Consequently, the reversible redox equilibria of Co(II)/(III), Zn(II)/(III), and Ni(II)/(III) (eq. (5)) in the tetrahedral sites of spinel structure built up a larger faradic pseudocapacitance than that of Mn(III)/(IV) and Pb(III)/Pb(IV) (eq. (6)) [44, 45].

$$MCo_2\,(OOH)_3 + e^- + H^+ \rightleftharpoons MCo_2O_4 + 2H_2 \ (M = Co,Zn,Ni) \tag{5}$$

$$MO_2 + e^- + H^+ \rightleftharpoons MOOH \ (M = Mn,Pb) \tag{6}$$

The relatively low Cpzc value of G, SnO/G, and IrO_2 must result of simple EDL behavior since there was no redox couple appeared during CV runs.

As shown in Fig. 4, there was a sharp increment in current as the potential was positively scanned to around +1.2 V, which was ascribed to water oxidation, i.e., the oxygen evolution reaction (OER), for all tested electrodes. The over-potential of OER was dependent on the electrode properties, which was critical to current efficiency of redox reaction in question. Typical feature of chloride redox reaction suggested that the anodic current of chloride oxidation (O_{Cl}) overlapped that of OER, whereas a corresponding cathodic peak current of chlorine reduction (R_{Cl}) was created when the potential was reversely scanned. In the presence of NaCl at specific concentration, O_{Cl} was accompanied by OER at around +1.0 V (vs. Ag/AgCl) and varied among MO/G electrodes due to different chlorine over-potentials intrinsic to each electrode. Since the peak faradaic current increased with increasing scan rate (Fig. S4 & S5), the redox reaction at specific chloride concentration could be explained by a Randles-Sevcik equation (eq. (7)) [46, 47], where the peak current, I_p, is a function of number of electron transferred (n), diffusion coefficient of chloride ion (D_{Cl}, cm^2/s)), scan rate (ν), electrode area (A), and bulk chloride concentration (C_0^*, mol/cm^3):

$$I_p = \left(2.69 \times 10^5\right) n^{\frac{3}{2}} D_{Cl}^{\frac{1}{2}} \nu^{\frac{1}{2}} A C_o^* \tag{7}$$

Fig. S5 shows the linear regression of I_{pc} (of R_{Cl}) versus chloride concentration which slope is a function of D_{Cl} at constant scan rate (10 mV/s). Table 3 shows that the diffusion coefficient of chloride ion is in the range of from 1.34×10^{-7} to 1.0×10^{-6} cm^2 s^{-1} on MO/G electrodes, which is similar to that on Pt/G electrode, 6.8×10^{-7} cm^2 s^{-1} [48]. D_{Cl} is an important physical parameter controlling the efficiency of simple diffusion-controlled electron transfer process [49], which is not substantially altered by different metal oxide electrodes herein. According to Eq. (7), when electron transfer is purely diffusion-controlled, a plot of logarithm peak cathodic current (log I_p) versus scan rate (log ν) will yield a slope of 0.5 [50, 51]. Fig. S6 examined the relationship between peak cathodic current and scan rate. Results showed that only graphite substrate (G) exhibited a slope of 0.53, while MnO/G, CoO/G, and CoNiO/G electrodes exhibited relatively large slope, which indicated that surface adsorption might affect the electrode kinetics of chlorine on these materials.

The linear region of polarization curve, log*I*, was plotted against applied potential, E, in the potential window of O_{Cl} reaction on the electrode surface as shown in Fig.S7. The Tafel slope b value is a function of 2.3RT/αnF (i.e., 0.059/nα V/dec at 298 K) [52, 53], from which the transfer coefficient (α) is obtained, assuming that the number of electron involved in Cl^-/Cl· transition (n) is 1. Although the chlorine oxidation signal, O_{Cl}, merged with that of water oxidation, i.e., OER, as shown in Fig. 4 (except IrO_2), the onset potential of chlorine, O_{Cl}, was lower than that of OER. Note that the calculation of a value for chloride oxidation was based on data in the low overpotential region according to the Tafel equation. Therefore, fortuitously, the α value for chloride oxidation was not affected by oxygen evolution. Table 3 also presents α value (based on the polarization data in Fig. S4). Transfer coefficient reflects the heterogeneous electrode kinetics within the Butler-Volmer formulation, and $0 < \alpha < 1$ for one electron process. When α equals 0.5, there is a symmetric form in the curvature of the Gibbs energy parabola of the reactant and product [54]. Accordingly, the transfer coefficient of chlorine on CoO/G (0.8), CoZnO/G (0.69), and CoNiO/G (0.67) were all greater than 0.5, which suggested that chloride redox reaction was favored over the spinel-type cobalt oxide electrode. It was noted that the C_{pzc} of metal oxide electrodes was positively correlated to α (or b value) (with a correlation coefficient $p = 0.931$). (Fig. S9). The effectiveness of electrocatalytic Cl^-/Cl· redox couple as well as the combination of Cl· intermediate should be affected by the electro-sorption of Cl^- . Anodic charging of the positively charged metal oxide surface balanced by the counter chloride ions is known to the primary mechanism of capacitive deionization (CDI) [55, 56]. In other words, Cl^- sorption in the electrical double-layer structure of the electrode surface occurred at a relatively low range of electrode potential benefited Cl_2 evolution at the over-potential of MO/G electrodes.

3.3. Batch chlorine yield and indirect electrochemical oxidation of ammonium ion

Figs. 5a and 5b give the chlorine production and current efficiency (η) of monometal oxide electrodes under constant current density of 3.5 mA/cm^2 and at 0.1 M [Cl^-] (prepared with synthetic seawater), respectively. Among all MO/G electrodes, CoO/G was the most effective in chlorine yield; in 60 min, the production of Cl_2 followed the order: CoO/G (57.2 mg/L) > PbO/G (19.1 mg/L) > MnO/G (14.7 mg/L) > SnO/G (8.67 mg/L) > *G* (8.07 mg/L) >> IrO_2/Ti (commercial DSA electrode, 0.01 mg/L). It is interesting that all MO/G electrodes exhibited chlorine yield greater than the commercial DSA. The current efficiency also followed the same order as that of chlorine yield; all electrodes exhibited current efficiency of less than 25% except CoO/G that attained a current efficiency of 69.4% at constant current of 3.5 mA cm^{-2} in 0.1-M NaCl solu-

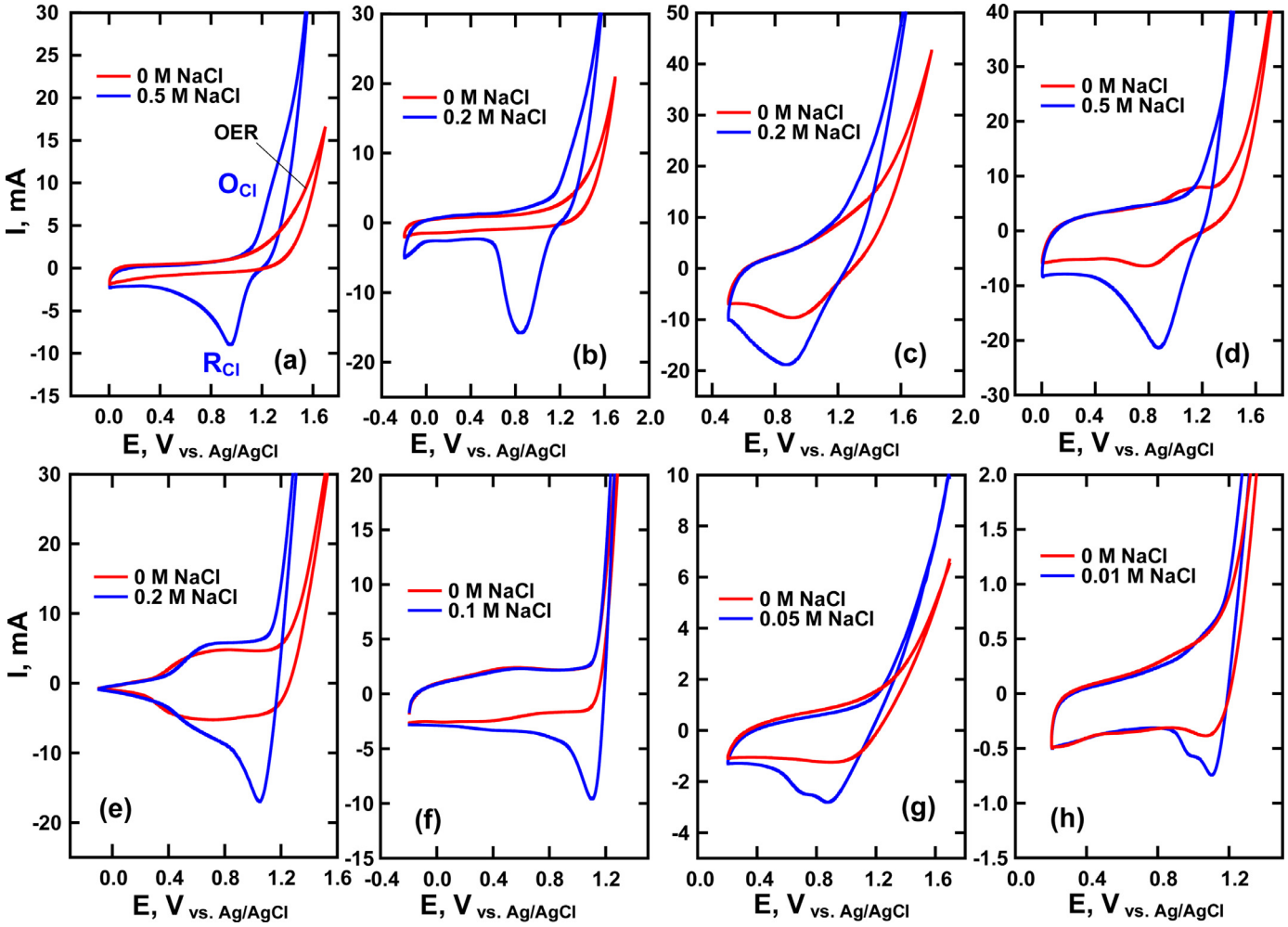

Fig. 4. Cyclic voltammetry of graphite-supported metal oxide electrodes: (a) G, (b) SnO/G, (c) PbO/G, (d) MnO/G, (e) CoO/G, (f) IrO_2/Ti, (g) CoZnO/G, (h) CoNiO/G, in the absence and presence of NaCl. (Reference electrode: Ag/AgCl, electrolyte = 0.1 M Na_2SO_4).

tion (Table S1). Because OER and chlorine overpotential (O_{Cl}) were overlapped with each other, the current derived from the electron transfer for $Cl^-/Cl\cdot$ declined when the electrode was not reactive in forming chlorine, so that the only side reaction of oxygen evolution became predominant. Fig. 5c gives the solution pH change with electrolytic time. The initial pH of the seawater, equivalent to 0.1 M [Cl^-], was 8.5–9, which slightly decreased to around 7.5 on CoO/G, while the pH sharply dropped to 3 on all other electrodes. Ideally, the anodic OER will create same quantity of hydrogen ions (eq. (8a)) as those consumed by the hydrogen evolution reaction (HER) on the cathode (eq. (8b)) [57].

$$2H_2O \rightarrow 4H^+ + 4e^- + O_2 \text{ (OER)} \quad (8a)$$

$$2H^+ + 2e^- \rightarrow H_2 \text{ (HER)} \quad (8b)$$

However, the current efficiency of OER and HER may differ on anode and cathode, respectively. In the present study, the electrochemical cell was asymmetric,that is, the counter electrode, graphite, was relatively inactive in transferring electrons for HER, thereby leading to a sharp drop in pH. The high current efficiency of CoO/G electrode in the chlorine yield suggests a smaller quantity of hydrogen ion evolved from the homogeneous hydrolysis of Cl_2 (eq. (9)) than OER (eq. (8a)), which was properly buffered by HER (eq. (8b)), leading to insignificant change in pH. In other words, the dissolved chlorine that quickly reacted with water near the anode maintained pH at neutral which was an indicator of chlorine being produced efficiently [58].

$$Cl_2 + 2H_2O \rightarrow HOCl + H^+ + Cl^- \quad (9)$$

In order to evaluate the kinetics of electrochemical chloride oxidation, the following equations were proposed as the overall mechanism on the MO/G surface (S) [59,60].

$$S + Cl^- (aq) \rightleftarrows SCl^- (ads);\ K_1 \text{ (fast chloride adsorption)} \quad (10a)$$

$$SCl^- \rightarrow SCl\bullet + e^-;\ k_2 \text{ (oxidation of adsorbed chloride)} \quad (10b)$$

$$2SCl\bullet \rightleftarrows SCl_2 + S;\ K_3 \text{ (chlorine formation)} \quad (10c)$$

$$SCl_2 \rightleftarrows S + Cl_2;\ K_4 \text{ (chlorine desorption)} \quad (10d)$$

Assuming that all surface adsorbed species are in the steady state, in terms of surface coverage, i.e.,θ_{Cl^-},$\theta_{Cl\cdot}$,θ_{Cl_2}, and the free site θ, one has: $\theta_{Cl^-} + \theta_{Cl\cdot} + \theta_{Cl_2} + \theta = 1$ and the rate of surface species change is zero, i.e., adsorption rate is commensurate to redox reaction rate. The concentration of surface $\theta_{Cl\cdot}$ is a function of chloride ion (eq. S2a): $\theta_{Cl^-} = \frac{k_1^+\theta}{k_2+k_1^-}[Cl^-]$. The rate equation of chloride ion [Cl^-] and chlorine [Cl_2] can be derived by the steady-state approach (eq. S3 and S4) and expressed as a function of electrolytic time:

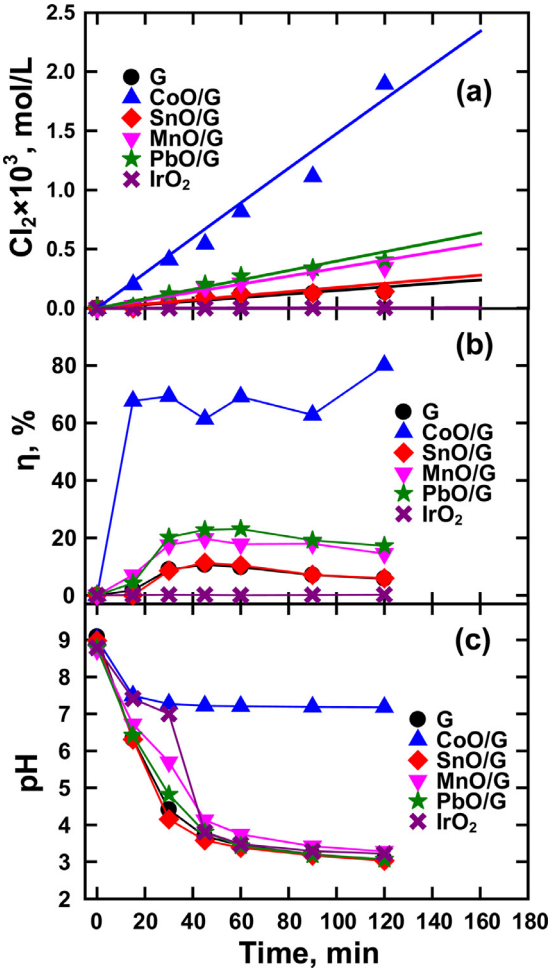

Fig. 5. (a) Chlorine yield, (b) current efficiency and (c) pH variation during chloride electrolysis over graphite and metal oxide electrodes ([Cl-] = 0.1 M; current density = 3.5 mA/cm^2).

$$\left[Cl^-\right] = \left[Cl^-\right]_0 e^{-k_{Cl}t} \tag{11}$$

$$[Cl_2] = \frac{1}{2}\left[Cl^-\right]_0\left(1 - e^{-k_{Cl}t}\right) \tag{12}$$

where. $k_{Cl} = \frac{k_1^+ k_2 \theta}{k_2 + k_1^-}$. Note that the rate constant, k_{Cl}, is a composite determined by rate of adsorption (k_1^+), rate of desorption (k_1^-), and the electron transfer for $Cl^-/Cl\cdot$ reaction (k_2). Table S1 lists the k_{Cl} value of all electrodes obtained by fitting the data shown in Fig. 5a using eq. (12). At 3.5 mA/cm^2 and 0.1 M [Cl^-], k_{Cl} of the CoO/G electrode (2.3×10^{-4} min^{-1}) was larger than that of all other MO/G electrodes, 8.0×10^{-5}, 6.8×10^{-5}, 3.5×10^{-5}, and 3.0×10^{-5} min^{-1} for PbO/G, MnO/G, SnO/G, and G, respectively. Fig. S7 shows the chlorine production as a function of time at different current density (0.5 – 3.5 mA/cm^2) and chloride concentrations (0.01 – 0.2 M) for the CoO/G, CoZnO/G and CoNiO/G electrode. Zn(II) and Ni(II) in bimetal oxides exhibited a synergistic effect on chlorine yield that increased with increasing current density. In 60 min, the chlorine concentration reached 57.2, 63.1, and 68.8 mg/L on CoO/G, CoNiO/G, and CoZnO/G electrode, respectively (Table S1). The current efficiency was increased from 69.4% on CoO/G to 76.2 and 83.1% on CoNiO/G and CoZnO/G, respectively. By contrast, increasing the initial [Cl^-] above 0.05 M in the synthetic seawater did not increased chlorine yield significantly. The extent of faradaic electron transfer played an important role on the yield of redox products. At constant current, once a fixed total charge ($Q = I \times t \times A$) was established, the current efficiency of Cl_2 production over a highly active electrocatalyst in different Cl^- concentrations will not change. Moreover, the concentration of chlorine was expected to increase with an increase in initial concentration of chloride ion. However, reaction between the Cl·and Cl^- to Cl_2^-·could occur at elevated chloride concentration [61,62]. Therefore, kinetically, the chlorine yield would be retarded by high concentration of chloride ion as shown in Table S1.

3.4. Electrochemical oxidation of ammonium ion

Fig. 6 shows the in situ chlorination of ammonium on MO/G electrodes in synthetic seawater ($[NH_4^+]_0$ = 20 mg-N/L or 1.42×10^{-3} M), $[Cl^-]_0$ = 0.05 M) at a constant current of 3.5 mA/cm^2. Results showed that at the onset of increase in chlorine concentration, the concentration of ammonium decreased. The cross-over time between the chlorine and ammonium concentration was around 90 and 200 min for CoO/G and PbO/G, respectively, which trend mimicked that of breakpoint chlorination to some extent. Since MnO/G and SnO/G had relatively low chlorine yield (Fig. 5a), no breakpoint chlorination seemed possible. Eilbeck reported that a stoichiometric ratio of 3:2 for $[Cl_2]$:$[NH_3]$ was needed to completely convert ammonia (NH_3) to nitrogen gas (N_2) [62]. At $[Cl_2]$:$[NH_3]$ ratio less than 3:2, i.e., pre-breakpoint chlorination, combined chlorines (chloramines) such as NH_2Cl, $NHCl_2$, and NCl_3 were formed, which still exhibited disinfection potential [63]. Less active electrodes, due to less chloride adsorption capability, required longer time to oxidize ammonium. Therefore, the cross-over time of chlorine, reflected the kinetics of ammonium oxidation. Moreover, the negligible concentration of nitrogen intermediates, such as NO_2^- and NO_3^-, during the entire course of electrolytic process proved indirect-electrochemical oxidation as mechanism of ammonium oxidation (Fig. S10) in which the consumption rate of $\Delta[Cl_2]/\Delta[NH_4^+]$ remained at around 1 to 1.2 before the cross-overtime of chlorine over ammonium occurred.

Fig. 7 shows results of ammonium oxidation in real aquaculture water (initial $[NH_4^+] \approx 3$ mg-N/L or 0.21×10^{-3} M, $[Cl^-]_0 \approx 0.37$ M) over cobalt oxide-based electrodes, namely, CoO/G, CoZnO/G, and CoNiO/G, as affected by applied current density (0.5, 2, and 3.5 mA/cm^2). Low ammonium removal efficiency of CoZnO/G at low current density (0.5 mA/cm^2) was attributable to the high chloride oxidation overpotential (i.e., the onset potential of CoZnO/G (1.2 V) > CoNiO/G (1.15 V) > CoO/G (1.0 V) (vs. Ag/AgCl), determined by the Tafel plot as shown in Fig. S8). However, with increasing current density up to 3.5 mA/cm^2, ammonium removal achieved 92.1% on CoZnO/G, which was higher than 84.1% and 61.2% on CoO/G and CoNiO/G, respectively, in 15 min; the residual NH_4^+-N (0.17 mg/L) was lowered to below the standard value regulated by Taiwan EPA for aquaculture water. Notably, breakpoint chlorination occurred at 15 min over all spinel oxides in treating real aquaculture water, compared to 90 min in treating synthetic seawater, on CoO/G electrode (Fig. 6), because of the difference in initial NH_4^+-N concentration, 3 mg/L (0.21×10^{-3} M) in real water vs. 20 mg/L (1.42×10^{-3} M) in synthetic seawater.

The surface reaction between the adsorbed NH_4^+ and chlorine radicals, *in-situ* generated by anodic oxidation of chloride ion, was supposed to be the primary mechanism of indirect-electrochemical ammonium ion oxidation eqs. (13) and (14) [64].

$$S + NH_4^+ \rightleftharpoons SNH_4^+;\ K_5 \tag{13}$$

$$6SCl^\bullet + SNH_4^+ \rightarrow SN_2 + 8SH^+;\ k_6 \tag{14}$$

where K_5 is the equilibrium constant of ammonium adsorption, and k_6 is the rate of indirect oxidation of ammonium by reactive chlorine species over the electrode surface. The coverage of two

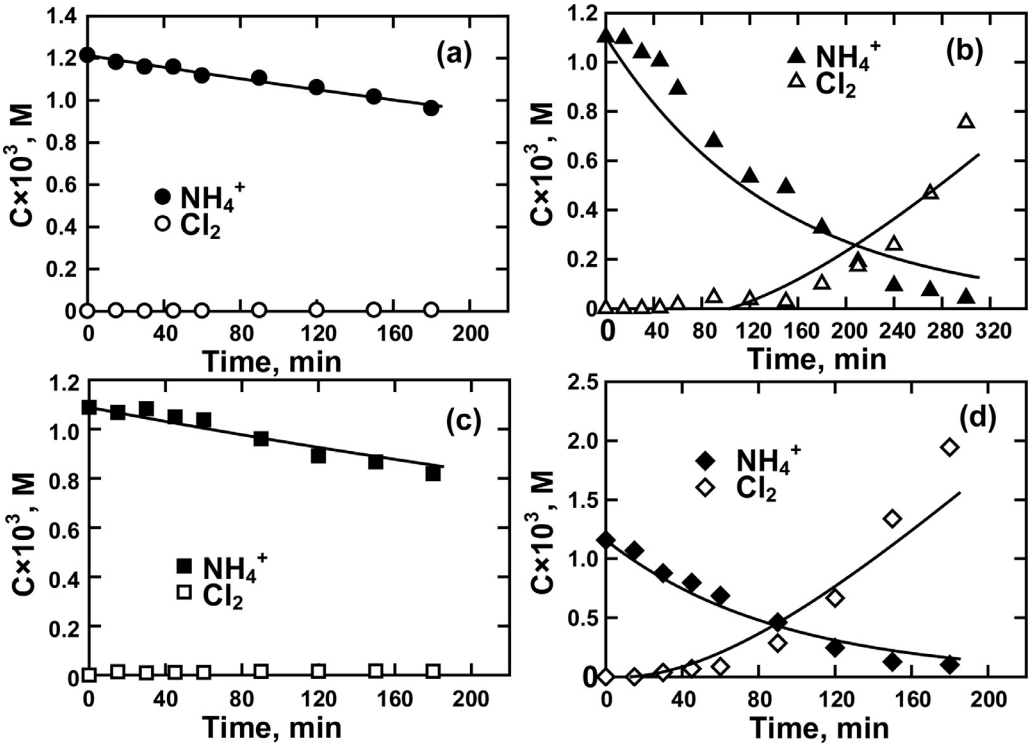

Fig. 6. Performance of (a) SnO/G, (b) PbO/G, (c) MnO/G and (d) CoO/G in ammonia oxidation and residual chlorine. ([NH_4^+]0 = 1.42 × 10^{-3} M (20 mg-N/L), [Cl^-] = 0.05 M; current density = 3.5 mA/cm^2).

surface species,$\theta_{Cl^-} = \frac{k_1^+\theta[Cl^-]+6k_6\theta_{Cl\cdot}\theta_{NH_4^+}}{k_1^-+k_2}$ and $\theta_{NH_4^+} = \frac{k_5^+\theta[NH_4^+]}{k_5^-+2k_6\theta_{Cl\cdot}}$ (eq. S7), were applied to derive the rate equation of ammonium ion oxidation and chlorine yield (eqs. S8 and S9). The detailed steady-state approach was provided in the Supporting Material. One can assume that the anodic oxidation of surface ammonium (k_6) is faster than the desorption of ammonium ion k_5^-, i.e., $\theta_{NH_4^+} \approx \frac{k_5^+\theta[NH_4^+]}{2k_6\theta_{Cl\cdot}}$, then the concentration profile of relevant NH_4^+ in the solution as a function of time can be obtained.

$$\frac{d[NH_4^+]}{dt} = -2k_6\theta_{Cl\cdot}\theta_{NH_4^+} = -k_N[NH_4^+], \quad (15a)$$

and

$$[NH_4^+] = [NH_4^+]_0 \exp^{-k_N t} \quad (15b)$$

where $k_N = k_5^+\theta$, which denotes the observed rate constant determined by the adsorption of ammonium ion. As a result, the rate constant k_N could be computed using the time function of chlorine yield according to the following equation:

$$[Cl_2] = \frac{1}{2}[Cl^-]_0\left(1 - e^{-k_{Cl}t}\right) - \frac{3}{2}K_{Cl}[NH_4^+]_0\left(1 - e^{-k_N t}\right) \quad (16)$$

where $K_{Cl} = \frac{k_1^-}{k_1^-+k_2}$ is the equilibrium constant between Cl^- desorption and oxidation. In contrast to the rate of chloride ion electrolysis according to eq. (12), the removal of NH_4^+ prolonged the time for chlorine production thereby extending the time of breakpoint chlorination (eq. (16)). Fig. 7d and 7e give k_{Cl} and k_N constants obtained by fitting data in Fig. 6 and Fig. 7, respectively. Results show that the rate constant, k_{Cl} was 2 orders of magnitude smaller than that of k_N, which indicated that chloride adsorption was the rate-determining step of ammonium oxidation. As for the electrochemical ammonium oxidation, k_{Cl} of CoO/G and PbO/G were 2.2 × 10^{-4} and 2.0 × 10^{-4} min^{-1}, respectively, which were even one order magnitude larger than that of MnO/G and SnO/G (2.3 × 10^{-5} and 1.4 × 10^{-5} min^{-1}, respectively). Besides, replacing Co(II) in the spinel structure of Co_3O_4 by Zn(II) and Ni(II), respectively, moderately improved the rate of chlorine yield over $ZnCo_3O$ and $NiCo_3O_4$ catalyst. The efficacy of NH_4^+ adsorption (k_5^+) was also high on cobalt oxide system due to its k_N value being larger than that of other metal oxides (1.1 × 10^{-2}, 7 × 10^{-3}, 1.35 × 10^{-3}, and 1.2 × 10^{-3} min^{-1} for CoO/G, PbO/G, MnO/G, and SnO/G, respectively). The rate constant k_N was improved in treating real aquaculture water (Fig. 7e) that contained lower ammonium ion concentration than the synthetic seawater. Nevertheless, on the basis of the rate of ammonium ion removal, which increased with increasing current density, CoZnO/G was the best electrode with k_N = 0.095 min^{-1} at current density of 3.5 mA/cm^2. Results of electroanalysis revealed that the pseudocapacitance of spinel oxides was superior to those of other metal oxides (Table 3), as the surface redox reactions was accelerated by enhancement in electro-sorption as reflected in capacitive charging.

Fig. 8 demonstrates the treatment of real aquaculture wastewater using a continuous flow reactor (Fig. S1c) to examine the durability of metal oxide electrodes and the feasibility of electrochemical remediation of solution containing ammonium ion. Results of batch experiments showed the breakpoint of chlorine yield occur at around 10 min, which resulted in greater than 90% of ammonium ion removal efficiency over CoZnO/G electrode (Fig. 8b). Thus, in continuous reaction, the flow rate selected was 5, 10, and 20 mL/min, corresponding to hydraulic retention time (HRT) of 5, 2.5, and 1.25 min, respectively (effective volume = 25 cm^3, anode = CoZnO/G, cathode = *G*). The effluent concentration of NH_4^+ and Cl_2 were recorded as a function of time (Fig. 8). The removal of ammonium ion and chlorine yield were maintained at above 99% and around 80 – 100 mg/L, respectively, for at least 48 h when the flow rate was 5 mL/min (or 5 min HRT). To minimize residual chlorine, one can reduce the HRT of the target reactants (Cl^- and NH_4^+) in the reactor. As the flow rate was increased to 10 and 20 mL/min (or HRT of 2.5 and 1.25 min), the effluent Cl_2 concentration was decreased to around 2 mg/L for both HRT, and the average NH_4^+ removal was 65 and 50%, for HRT of 2.5 and

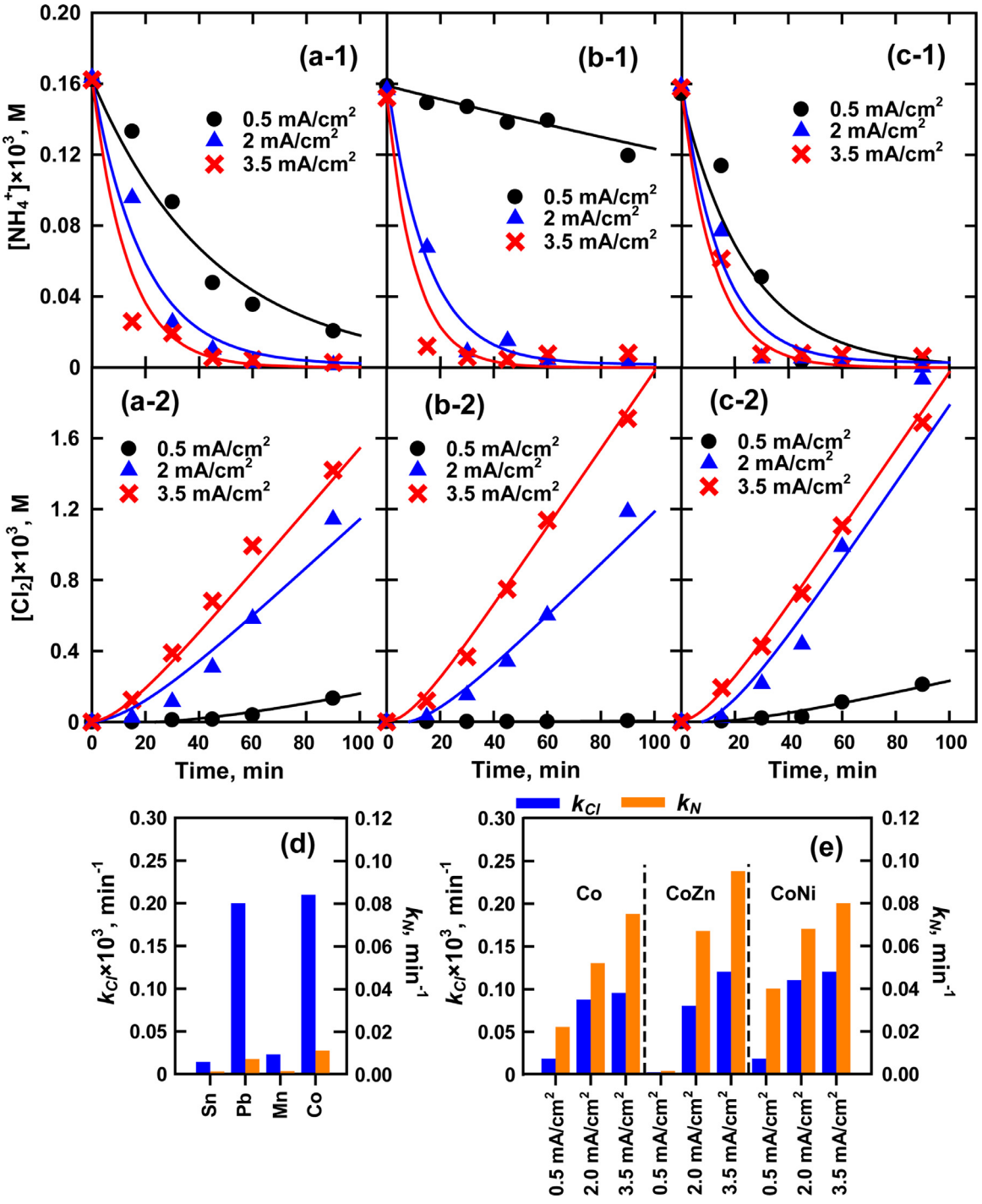

Fig. 7. Performance of (a) CoO/G, (b) CoZnO/G, and (c) CoNiO/G in 1. Ammonia oxidation, and 2. Chlorine yield of real aquaculture water under 0.5–3.5 mA/cm^2; Rate constants, k_{Cl} and kN, over MO/G electrodes in (d) synthetic seawater ($[NH_4^+]_0 = 1.42 \times 10^{-3}$ M (20 mg-N/L), $[Cl^-]_0 = 0.1$ M, 3.5 mA/cm^2), and (e) real aquaculture water at different current density ($[NH^{4+}]_0 \approx 0.21 \times 10^{-3}$ M (3 mg-N/L), $[Cl^-]_0 = 0.37$ M).

1.25 min, respectively. The result of continuous flow runs implied that the level of ammonium nitrogen outflow, for recirculation to aquaculture system, could be readily controlled by HRT. Moreover, active electrocatalysts capable of rapid chlorine generation, is key to shorten the hydraulic retention time in wastewater treatment with increasing treatment capacity.

Conclusion

Six metal oxide electrodes, including mono-metal (Sn, Mn, Pb, and Co) and bimetal (CoZn and CoNi) on graphite plate support, were studied for the removal of ammonium in aquaculture wastewater by indirect electrochemical oxidation. The MO/G electrodes, synthesized by electrodepostion using metal tartrate precursor in alkaline solution (pH 12), were characterized as metal dioxides of SnO_2, MnO_2, and PbO_2 and spinel oxides, namely, Co_3O_4, $ZnCo_2O_4$, and $NiCo_2O_4$. The CoO/G electrode exhibited excellent activity in chlorine yield, ascribed to fast transfer coefficient and presence of pseudocapacitance, thereby outperforming other dioxide electrodes. Substitution of Co(II) by Ni(II) and Zn(II) in spinel oxides exhibited synergistic effect on chloride electrolysis, which enhanced electrochemical removal of ammonium. The per-

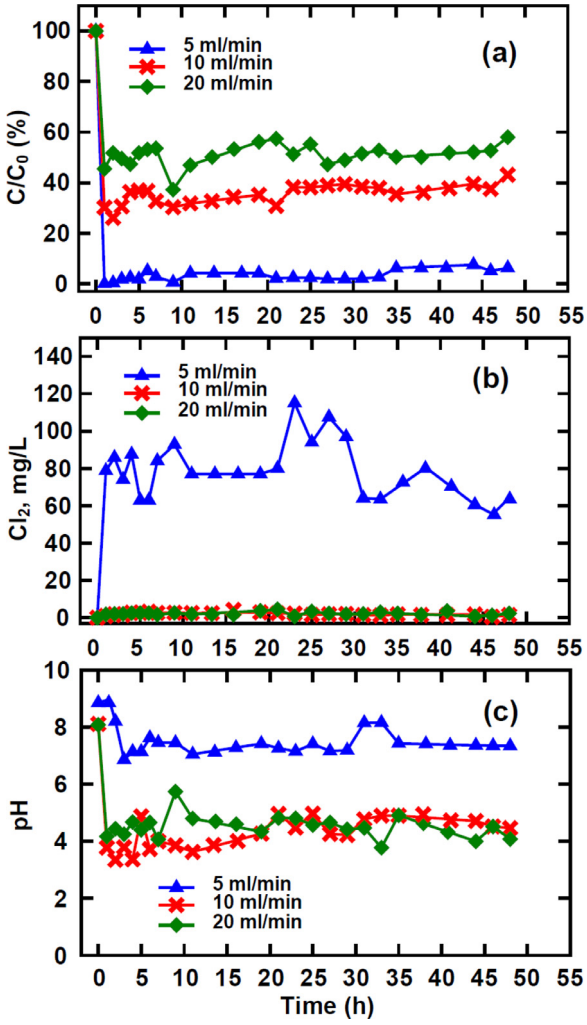

Fig. 8. Effect of flow rate on ammonia oxidation, chloride yield and pH variation in a continuous electrochemical reactor using CoZnO/G and G as anode and cathode, respectively (current density = 3.5 mA/cm^2).

formance of MO/G electrodes, in terms of change of Cl_2 and NH_4^+ concentration, could be readily verified by the significant shortening of electrolytic time toward breakpoint of free Cl_2. Therefore, the hydraulic retention time will be a useful operational parameter for controlling the residual free chlorine and the conversion of NH_4^+ in the effluent of continuous-flow-through electrochemical reactor for recirculation of the treated wastewater to the fishing pond.

Declaration of Competing Interest

None.

CRediT authorship contribution statement

Yu-Jen Shih: Writing - original draft, Formal analysis, Project administration, Supervision, Funding acquisition. **Shih-Hsuan Huang:** Resources, Data curation. **Ching-Lung Chen:** Resources, Visualization. **Cheng-Di Dong:** Resources, Visualization. **Chin-Pao Huang:** Conceptualization, Writing - review & editing.

Acknowledgment

The authors would like to thank the Ministry of Science and Technology, Taiwan for generous finance support of this research under Contract No. MOST 108-2628-E-110 - 005 - MY3. Addition support was provided by US NSF IOA (1632899) to CPH.

Supplementary materials

Supplementary material associated with this article can be found, in the online version, at doi:10.1016/j.electacta.2020.136990.

References

[1] V. Díaz, R. Ibáñez, P. Gómez, A.M. Urtiaga, I. Ortiz, Kinetics of electro-oxidation of ammonia-N, nitrites and COD from a recirculating aquaculture saline water system using BDD anodes, Water Res. 45 (1) (2011) 125–134, doi:10.1016/j.watres.2010.08.020.
[2] F. Bernardi, I.V. Zadinelo, H.J. Alves, F. Meurer, L.D. dos Santos, Chitins and chitosans for the removal of total ammonia of aquaculture effluents, Aquaculture 483 (20) (2018) 203–212, doi:10.1016/j.aquaculture.2017.10.027.
[3] R.D. Zweig, J.D. Morton, M.M. Stewart, Source Water Quality for Aquaculture, The World Bank, Washington, D.C., 1999.
[4] M. Kır, M. Can, S. Mehmet, G. Gök, Acute ammonia toxicity and the interactive effects of ammonia and salinity on the standard metabolism of European sea bass (Dicentrarchuslabrax), Aquaculture 511 (2019) 734273, doi:10.1016/j.aquaculture.2019.734273.
[5] W.T. Mook, M.H. Chakrabarti, M.K. Aroua, G.M.A. Khan, B.S. Ali, M.S. Islam, M.A. Abu Hassan, Removal of total ammonia nitrogen (TAN), nitrate and total organic carbon (TOC) from aquaculture wastewater using electrochemical technology: a review, Desalination 285 (2012) 1–13, doi:10.1016/j.desal.2011.09.029.
[6] T.J. Park, J.H. Lee, M.S. Lee, C.H. Park, C.H. Lee, S.D. Moon, J. Chung, R. Cui, Y.J. An, D.H. Yeom, S.H. Lee, J.K. Lee, K.D. Zoh, Development of water quality criteria of ammonia for protecting aquaticlife in freshwater using species sensitivity distribution method, Sci. Total Environ. 634 (1) (2018) 934–940, doi:10.1016/j.scitotenv.2018.04.018.
[7] M.O. Rivett, S.R. Buss, P. Morgan, J.W.N. Smith, C.D. Bemment, Nitrate attenuation in groundwater: a review ofbiogeochemical controlling processes, Water Res. 42 (2008) 4215–4232, doi:10.1016/j.watres.2008.07.020.
[8] J. Lee, I.S. Kim, A. Emmanuel, S.C. Koh, Microbial valorization of solid wastes from a recirculating aquaculture system and the relevant microbial functions, Aquacul. Eng. 87 (2019) 102016, doi:10.1016/j.aquaeng.2019.102016.
[9] K.Drønen Roalkvam, H. Dahle, H.I. Wergeland, Comparison of active biofilm carriers and commercially available inoculum for activation of biofilters in marine recirculating aquaculture systems (RAS), Aquaculture 514 (1) (2020) 734480, doi:10.1016/j.aquaculture.2019.734480.
[10] S. Hosseinzadeh, G. Bonarrigo, Y. Verheust, P. Roccaro S.V. Hulle, Water reuse in closed hydroponic systems: comparison of GAC adsorption, ion exchange and ozonation processes to treat recycled nutrient solution, Aquacul. Eng. 78-B (2017) 190–195, doi:10.1016/j.aquaeng.2017.07.007.
[11] T.D.P. Nguyen, T.N.T. Tran, T.V.A. Le, T.X.N. Phan, P.L. Show, Chia S.R, Autoflocculation through cultivation of Chlorella vulgaris in seafood wastewater discharge: influence of culture conditions on microalgae growth and nutrient removal, J. Biosci. Bioeng. 127 (4) (2019) 492–498, doi:10.1016/j.jbiosc.2018.09.004.
[12] P.A. Krisbiantoro, T. Togawa, L. Mahardiani, H. Aihara, R. Otomo, Y. Kamiya, The role of cobalt oxide or magnesium oxide in ozonation of ammonia nitrogen in water, Appl. Catal. A 596 (2020) 117515, doi:10.1016/j.apcata.2020.117515.
[13] X. Tan I. Acquah, H. Liu, W. Lie, S. Tan, A critical review on saline wastewater treatment by membrane bioreactor (MBR) from a microbial perspective, Chemosphere 220 (2019) 1150–1162, doi:10.1016/j.chemosphere.2019.01.027.
[14] K. Endo, K. Nakamura, Y. Katayama, T. Miura, Pt–Me (Me = Ir, Ru, Ni) binary alloys as an ammonia oxidation anode, Electrochim. Acta 49 (2004) 2503–2509, doi:10.1016/j.electacta.2004.01.025.
[15] M.F. Ezzat, I. Dincer, Energy and exergy analyses of a novel ammonia combined power plant operating with gas turbine and solid oxide fuel cell systems, Energy 194 (2020) 116750, doi:10.1016/j.energy.2019.116750.
[16] S. Johnston, B.H.R. Suryanto, D.R. MacFarlane, Electro-oxidation of ammonia on electrochemically roughened platinum electrodes, Electrochim. Acta 297 (20) (2019) 778–783, doi:10.1016/j.electacta.2018.12.014.
[17] Y.J. Shih, Y.H. Huang, C.P. Huang, Oxidation of ammonia in dilute aqueous solutions over graphite-supported a- and b-lead dioxide electrodes (PbO_2@G), Electrochim. Acta 257 (2017) 444–454, doi:10.1016/j.electacta.2017.10.060.
[18] Y.J. Shih, Y.H. Huang, C.P. Huang, Electrocatalytic ammonia oxidation over a nickel foam electrode: role of $Ni(OH)_{2(s)}$-$NiOOH_{(s)}$ nanocatalysts, Electrochim. Acta 263 (2018) 261–271, doi:10.1016/j.electacta.2018.01.045.
[19] Y. Gendel, O. Lahav, Revealing the mechanism of indirect ammonia electrooxidation, Electrochim. Acta 63 (2012) 209–219, doi:10.1016/j.electacta.2011.12.092.
[20] C. Zhang, D. He, J. Ma, T.D. Waite, Active chlorine mediated ammonia oxidation revisited: reaction mechanism, kinetic modelling and implications, Water Res. 145 (2018) 220–230, doi:10.1016/j.watres.2018.08.025.
[21] H. Over, Surface chemistry of ruthenium dioxide in heterogeneous catalysis and electrocatalysis: from fundamental to applied research, Chem. Rev. 2012 (112) (2012) 3356–3426, doi:10.1021/cr200247n.

[22] T. Le Luu, J. Kim, J. Yoon, Physicochemical properties of RuO_2 and IrO_2 electrodes affecting chlorine evolutions, J. Ind. Eng. Chem. 21 (2015) 400–404, doi:10.1016/j.jiec.2014.02.052.

[23] J. Kim, C. Kim, S. Kim, J. Yoon, RuO_2 coated blue TiO_2 nanotube array (blue TNA-RuO_2) as an effective anode material in electrochemical chlorine generation, J. Ind. Eng. Chem. 66 (2018) 478–483, doi:10.1016/j.jiec.2018.06.015.

[24] H. Ma, W.F. Schneider, DFT and microkinetic comparison of Pt, Pd and Rh-catalyzed ammonia oxidation, J. Catal. 383 (2020) 322–330, doi:10.1016/j.jcat.2020.01.029.

[25] M. Rajab, C. Heim, T. Letzel, J.E. Drewes, B. Helmreich, Electrochemical disinfection using boron-doped diamond electrode –The synergetic effects of in situ ozone and free chlorine generation, Chemosphere 121 (2015) 47–53, doi:10.1016/j.chemosphere.2014.10.075.

[26] K. Hara, N. Kishimoto, M. Kato, H. Otsu, Efficacy of a two-compartment electrochemical flow cell introduced into a reagent-free UV/chlorine advanced oxidation process, Chem. Eng. J. 388 (2020) 124385, doi:10.1016/j.cej.2020.124385.

[27] N. Gedam, N.R. Neti, M. Kormunda, J. Subrt, S. Bakardjieva, Novel lead dioxide-graphite-polymer composite anode for electrochemical chlorine generation, Electrochim. Acta 169 (2015) 109–116, doi:10.1016/j.electacta.2015.04.058.

[28] P. Mandal, A.K. Gupta, B.K. Dubey, Role of inorganic anions on the performance of landfill leachate treatment by electrochemical oxidation using graphite/PbO_2 electrode, J. Water Proc. Eng. 33 (2020) 101119, doi:10.1016/j.jwpe.2019.101119.

[29] C.M. Chung, S.W. Hong, K. Cho, M.R. Hoffmann, Degradation of organic compounds in wastewater matrix by electrochemically generated reactive chlorine species: kinetics and selectivity, Catal. Today 313 (2018) 189–195, doi:10.1016/j.cattod.2017.10.027.

[30] J. Wang, J. Ge, H. Hou, M. Wang, G. Liu, G. Qiao, Y. Wang, Design and sol-gel preparation of SiO_2/TiO_2 and $SiO_2/SnO_2/SiO_2$-SnO_2 multilayer antireflective coatings, Appl. Surf. Sci. 422 (2017) 970–974, doi:10.1016/j.apsusc.2017.06.133.

[31] J. Kim, C. Kim, S. Kim, J. Yoon, RuO_2 coated blue TiO_2 nanotube array (blue TNA-RuO_2) as an effective anode material in electrochemical chlorine generation, J. Ind. Eng. Chem. 66 (2018) 478–483, doi:10.1016/j.jiec.2018.06.015.

[32] B. Bakheet, J. Beardall, X. Zhang, D. McCarthy, What is the efficiency of electrogeneration of chlorine with a solid polymer electrolyte assembly? Chem. Eng. J. 364 (2019) 370–375, doi:10.1016/j.cej.2019.01.174.

[33] P. Li, T. Yoshimura, T. Furuta, T. Yanagawa, K. Shiozaki, T. Kobayashi, Sunlight caused interference in outdoor N, N-diethyl-p-phenylenediamine colorimetric measurement for residual chlorine and the solution for on-site work, Ecotoxicol. Environ. Saf. 169 (2019) 640–644, doi:10.1016/j.ecoenv.2018.11.055.

[34] Y.B. Cho, S.H. Jeong, H. Chun, Y.S. Kim, Selective colorimetric detection of dissolved ammonia in water via modified Berthelot's reaction on porous paper, Sens. Actuat. B-Chem. 256 (2018) 167–175, doi:10.1016/j.snb.2017.10.069.

[35] J.J.M. Vequizo, J. Wang, M. Ichimura, Electrodeposition of SnO_2 thin films from aqueous tin sulfate solutions, Japan. J. Appl. Phys. 49 (2010) 125502.

[36] J. Linnemann, L. Taudien, M. Klose, L. Giebeler, Electrodeposited films to MOF-derived electrochemical energy storage electrodes: a concept of simplified additive-free electrode processing for self-standing, ready-to-use materials, J. Mater. Chem. A 5 (2017) 18420, doi:10.1039/C7TA01874F.

[37] J.A. Koza, Z. He, A.S. Miller, J.A. Switzer, Electrodeposition of crystalline Co_3O_4-a catalyst for the oxygen evolution reaction, Chem. Mater. 24 (2012) 3567–3573, doi:10.1021/cm3012205.

[38] V. Kumar, C.R. Mariappan, R. Azmi, D. Moock, S. Indris, M. Bruns, H. Ehrenberg, G.V. Prakash, Pseudocapacitance of mesoporous spinel-Type MCo_2O_4 (M = Co, Zn, and Ni) rods fabricated by a facile solvothermal route, ACS Omega 2 (2017) 6003–6013, doi:10.1021/acsomega.7b00709.

[39] M. Fondell, M. Gorgoi, M. Boman, A. Lindblad, An HAXPES study of Sn, SnS, SnO and SnO_2, J. Electron. Spectrosc. 195 (2014) 195–199, doi:10.1016/j.elspec.2014.07.012.

[40] M.C. Biesinger, B.P. Payne, A.P. Grosvenor, L.W.M. Lau, A.R. Gerson, R.S.C. Smart, Resolving surface chemical states in XPS analysis of first row transition metals, oxides and hydroxides: cr, Mn, Fe, Co and Ni, Appl. Surf. Sci. 257 (2011) 2717–2730, doi:10.1016/j.apsusc.2010.10.051.

[41] K.Sharm Poonam, A. Arora, S.K. Tripathi, Review of supercapacitors: materials and devices, J. Energy Stor. 21 (2019) 801–825, doi:10.1016/j.est.2019.01.010.

[42] L. Guan, L. Yu, G.Z. Chen, Capacitive and non-capacitive faradaic charge storage, Electrochim. Acta 206 (2016) 464–478, doi:10.1016/j.electacta.2016.01.213.

[43] M. Käärik, M. Arulepp, M. Käärik, U. Maran, J. Leis, Characterization and prediction of double-layer capacitance of nanoporous carbon materials using the Quantitative nano-Structure-Property Relationship approach based on experimentally determined porosity descriptors, Carbon N Y 158 (2020) 494–504, doi:10.1016/j.carbon.2019.11.017.

[44] P.R. Bandaru, H. Yamada, R. Narayanan, M. Hoefer, Charge transfer and storage in nanostructures, Mater. Sci. Eng. R. 96 (2015) 1–69, doi:10.1016/j.mser.2015.06.001.

[45] S.K. Chang, Z. Zainal, K.B. Tan, N.A. Yusof, W.M.D.W. Yusoff, S.R.S. Prabaharan, Recent development in spinel cobaltites for supercapacitor application, Ceram. Intern. 41 (1) (2015) 1–14, doi:10.1016/j.ceramint.2014.07.101.

[46] J. Muñoz, Céspedes F., M. Baeza, Modified multiwalled carbon nanotube/epoxy amperometric nanocomposite sensors with CuO nanoparticles for electrocatalytic detection of free chlorine, Microchem. J. 122 (2015) 189–196, doi:10.1016/j.microc.2015.05.001.

[47] V. Usai, T. Mugadza, F. Chigondo, M. Shumba, T. Nharingo, M. Moyo, Tshuma P., Synthesis and characterisation of cobalt oxide nanoparticles decoratedgraphene oxide and its electrocatalytic behavior, Polyhedron 157 (2019) 192–199, doi:10.1016/j.poly.2018.10.002.

[48] Y.J. Shih, C.C. Su, C.P. Huang, The synthesis, characterization, and application of a platinum modified graphite electrode (Pt/G) exemplified by chloride oxidation, Sep. Purif. Technol. 156 (2015) 961–971, doi:10.1016/j.seppur.2015.09.045.

[49] M. Bogdan, D. Brugger, W. Rosenstie, B. Speiser, Estimation of diffusion coefficients from voltammetric signals by support vector and gaussian process regression, J. Cheminform 6 (2014) 30, doi:10.1186/1758-2946-6-30.

[50] M. Diaz, M. Cataldo, P. Ledezma, J. Keller, K. Doederer, Unravelling the mechanisms controlling the electro-generation of ferrate using four iron salts in boron-doped diamond electrodes, J. Electroanal. Chem. 854 (2019) 113501, doi:10.1016/j.jelechem.2019.113501.

[51] C. Heyser, R. Schrebler, P. Grez, New route for the synthesis of nickel (II) oxide nanostructures and its application as non-enzymatic glucose sensor, J. Electroanal. Chem. 832 (2019) 189–195, doi:10.1016/j.jelechem.2018.10.054.

[52] A.P.S. Gaur, B. Zhang, Y.H. Lui, X. Tang, S. Hu, Morphologically tailored nanostructured MoS_2 catalysts via introduction of Ni and Co ions for enhanced HER activity, Appl. Surf. Sci. 516 (2020) 146094, doi:10.1016/j.apsusc.2020.146094.

[53] D.N. Sangeeth, M.S. Santosh, M. Selvakumar, Flower-like carbon doped MoS_2/Activated carbon composite electrode for superior performance of supercapacitors and hydrogen evolution reactions, J. Alloy. Compd 831 (2020) 154745, doi:10.1016/j.jallcom.2020.154745.

[54] H. Chen, J.R. Elliott, H. Le, M. Yang, R.G. Compton, Super-Nernstian Tafel slopes: an origin in coupled homogeneous kinetics, J. Electroanal. Chem. 869 (2020) 114185, doi:10.1016/j.jelechem.2020.114185.

[55] S. Porada, R. Zhao, A. van der Wal, V. Presser, P.M. Biesheuvel, Review on the science and technology of water desalination by capacitive deionization, Prog. Mater. Sci. 58 (8) (2013) 1388–1442, doi:10.1016/j.pmatsci.2013.03.005.

[56] J. Huang, M. Hou, J. Wang, X. Teng, Niu M.Xu Y., Z. Chen, RuO_2 nanoparticles decorate belt-like anatase TiO2for highly efficient chlorine evolution, Electrochim. Acta 339 (2020) 135878, doi:10.1016/j.electacta.2020.135878.

[57] S. Chandrasekaran, D. Ma, Y. Ge, L. Deng, C. Bowen, J. Roscow, Y. Zhang, Z. Lin, R.D.K. Misra, J. Li, P. Zhang, H. Zhang, Electronic structure engineering on two-dimensional (2D) electrocatalytic materials for oxygen reduction, oxygen evolution, and hydrogen evolution reactions, Nano Energy 77 (2020) 105080, doi:10.1016/j.nanoen.2020.105080.

[58] D. Ghernaout, Naceur M.W, A. Aouabed, On the dependence of chlorine by-products generated species formation of theelectrode material and applied charge during electrochemical water treatment, Desalination 270 (1–3) (2011) 9–22, doi:10.1016/j.desal.2011.01.010.

[59] S.O. Ganiyu, M.G. El-Din, Insight into in-situ radical and non-radical oxidative degradation of organic compounds in complex real matrix during electrooxidation with boron doped diamond electrode: a case study of oil sands process water treatment, Appl. Catal. B-Environ. 279 (2020) 119366, doi:10.1016/j.apcatb.2020.119366.

[60] S. Bekkouche, S. Merouani, O. Hamdaoui, M. Bouhelassa, Efficient photocatalytic degradation of Safranin O by integrating solar-UV/TiO_2/persulfate treatment: implication of sulfate radical in the oxidation process and effect of various water matrix components, J. Photochem. Photobio. A: Chem. 345 (2017) 80–91, doi:10.1016/j.jphotochem.2017.05.028.

[61] F.Z. Meghlaoui, S. Merouani, O. Hamdaoui, M. Bouhelassa, M. Ashokkumar, Rapid catalytic degradation of refractory textile dyes in Fe(II)/chlorine system at near neutral pH: radical mechanism involving chlorine radical anion ($Cl_2^{\cdot-}$)-mediated transformation pathways and impact of environmental matrices, Sep. Purif. Technol. 227 (2019) 115685, doi:10.1016/j.seppur.2019.115685.

[62] W.J. Eilbeck, Redox control in breakpoint chlorination of ammonia and metal ammine complexes, Water Res. 18 (1984) 21–24, doi:10.1016/0043-1354(84)90043-5.

[63] E. Lacasa, J. Llanos, P. Canizares, M.A. Rodrigo, Electrochemical denitrificacion with chlorides using DSA and BDD anodes, Chem. Eng. J. 184 (2012) 66–71, doi:10.1016/j.cej.2011.12.090.

[64] Y. Gendel, O. Lahav, Revealing the mechanism of indirect ammonia electrooxidation, Electrochim. Acta 63 (2012) 209–219, doi:10.1016/j.electacta.2011.12.092.